Research Article | Vol. 8, No. 7 | 1 Jul 2018 | OPTICAL MATERIALS EXPRESS 1890
Optical Materials EXPRESS

Three-dimensional beam-splitting transitions and numerical modelling of direct-laser-written near-infrared $LiNbO_3$ cladding waveguides

JAVIER G. AJATES,[1,2] JAVIER R. VÁZQUEZ DE ALDANA,[1,*] FENG CHEN,[3] AND AIRÁN RÓDENAS[4]

[1]*Grupo de Investigación en Aplicaciones del Láser y Fotónica, University of Salamanca, Pl. La Merced SN, E-37008 Salamanca, Spain*
[2]*Spanish Center for Pulsed Lasers, M5 Bldg., Science Park, Villamayor, Salamanca, Spain*
[3]*School of Physics, Shandong University, 250100 Jinan, Shandong, China*
[4]*Istituto di Fotonica e Nanotecnologie (IFN) - Consiglio Nazionale delle Ricerche (CNR), Piazza Leonardo da Vinci 32, 20133 Milano, Italy*
**jrval@usal.es*

Abstract: We report novel results on the fabrication of near-infrared waveguides inside lithium niobate ($LiNbO_3$) crystals with different three-dimensional beam-splitting architectures, comparing the effects that each type of architecture has on the propagation losses and mode evolutions. Optimized waveguides are then studied in detail to obtain the refractive index profiles within the femtosecond-laser-written claddings with sub-micron resolution. This knowledge is currently impossible to obtain with experimental techniques and allows for the proper understanding of the laser-writing process, as well as to design novel waveguides and photonic circuits with optimized properties.

OCIS codes: (130.3120) Integrated optics devices; (130.3730) Lithium niobate; (140.3390) Laser materials processing; (230.7380) Waveguides, channeled; (000.4430) Numerical approximation and analysis.

References and links

1. A. Okhrimchuk, V. Mezentsev, A. Shestakov, and I. Bennion, "Low loss depressed cladding waveguide inscribed in YAG:Nd single crystal by femtosecond laser pulses," Opt. Express **20**(4), 3832–3843 (2012).
2. F. Chen and J. R. Vázquez de Aldana, "Optical waveguides in crystalline dielectric materials produced by femtosecond-laser micromachining," Laser Photonics Rev. **8**(2), 251–275 (2014).
3. Y. Ren, G. Brown, R. Mary, G. Demetriou, D. Popa, F. Torrisi, A. C. Ferrari, F. Chen, and A. K. Kar, "7.8-GHz Graphene-Based 2-μm Monolithic Waveguide Laser," IEEE J. Sel. Top. Quantum Electron. **21**(1), 1602106 (2015).
4. H. D. Nguyen, A. Ródenas, J. R. Vázquez de Aldana, J. Martínez, F. Chen, M. Aguiló, M. C. Pujol, and F. Díaz, "Heuristic modelling of laser written mid-infrared $LiNbO_3$ stressed-cladding waveguides," Opt. Express **24**(7), 7777–7791 (2016).
5. A. Ródenas, G. A. Torchia, G. Lifante, E. Cantelar, J. Lamela, F. Jaque, L. Roso, and D. Jaque, "Refractive index change mechanisms in femtosecond laser written ceramic Nd:YAG waveguides: micro-spectroscopy experiments and beam propagation calculations," Appl. Phys. B **95**(1), 85–96 (2009).
6. J. Ajates, C. Romero, G. Castillo, F. Chen, and J. R. Vázquez de Aldana, "Y-junctions based on circular depressed-cladding waveguides fabricated with femtosecond pulses in Nd:YAG crystal: A route to integrate complex photonic circuits in crystals," Opt. Mater. **72**, 220–225 (2017).
7. E. Kifle, X. Mateos, J. R. de Aldana, A. Ródenas, P. Loiko, S. Y. Choi, F. Rotermund, U. Griebner, V. Petrov, M. Aguiló, and F. Díaz, "Femtosecond-laser-written Tm:$KLu(WO_4)_2$ waveguide lasers," Opt. Lett. **42**(6), 1169–1172 (2017).
8. Y. Jia, J. R. Vázquez de Aldana, C. Romero, Y. Ren, Q. Lu, and F. Chen, "Femtosecond-Laser-Inscribed BiB_3O_6 Nonlinear Cladding Waveguide for Second-Harmonic Generation," Appl. Phys. Express **5**(7), 072701 (2012).
9. R. Osellame, G. Cerullo, and R. Ramponi, *Femtosecond Laser Micromachining: Photonic and Microfluidic Devices in Transparent Materials* (Springer Science & Business Media, 2012).
10. D. Choudhury, J. Macdonald, and A. K. Kar, "Ultrafast laser inscription: perspectives on future integrated applications," Laser Photonics Rev. **8**(6), 827–846 (2014).

#330293 https://doi.org/10.1364/OME.8.001890
Journal © 2018 Received 25 Apr 2018; revised 18 May 2018; accepted 26 May 2018; published 13 Jun 2018

Optical Materials EXPRESS

11. Y. Liao, J. Xu, Y. Cheng, Z. Zhou, F. He, H. Sun, J. Song, X. Wang, Z. Xu, K. Sugioka, and K. Midorikawa, "Electro-optic integration of embedded electrodes and waveguides in $LiNbO_3$ using a femtosecond laser," Opt. Lett. **33**(19), 2281–2283 (2008).
12. A. Ródenas, G. Martin, B. Arezki, N. Psaila, G. Jose, A. Jha, L. Labadie, P. Kern, A. Kar, and R. Thomson, "Three-dimensional mid-infrared photonic circuits in chalcogenide glass," Opt. Lett. **37**(3), 392–394 (2012).
13. Y. Okamura, S. Yoshinaka, and S. Yamamoto, "Measuring mode propagation losses of integrated optical waveguides: a simple method," Appl. Opt. **22**(23), 3892–3894 (1983).
14. A. Ródenas, J. A. Sanz Garcia, D. Jaque, G. A. Torchia, C. Mendez, I. Arias, L. Roso, and F. Agullo-Rueda, "Optical investigations of femtosecond laser induced microstress in neodymium doped lithium niobate crystals," J. Appl. Phys. **100**(3), 033521 (2006).
15. A. Ródenas, L. M. Maestro, M. Ramirez, G. A. Torchia, L. Roso, F. Chen, and D. Jaque, "Anisotropic lattice changes in femtosecond laser inscribed Nd^{3+}:MgO:$LiNbO_3$ optical waveguides," J. Appl. Phys. **106**(1), 013110 (2009).
16. H.-D. Nguyen, A. Ródenas, J. R. Vázquez de Aldana, G. Martín, J. Martínez, M. Aguiló, M. C. Pujol, and F. Díaz, "Low-loss 3D-laser-written mid-infrared depressed-index cladding waveguides for both TE and TM polarizations," Opt. Express **25**(4), 3722–3736 (2017).
17. T. Calmano, C. Kränkel, and G. Huber, "Laser oscillation in Yb:YAG waveguide beam-splitters with variable splitting ratio," Opt. Lett. **40**(8), 1753–1756 (2015).
18. J. Burghoff, C. Grebing, S. Nolte, and A. Tünnermann, "Efficient frequency doubling in femtosecond laser written waveguides in lithium niobate," Appl. Phys. Lett. **89**(8), 081108 (2006).

1. Introduction

Three-dimensional direct laser writing (3DLW) of depressed cladding waveguides (CWs) [1] in crystalline optical materials has received tremendous attention in recent years (see [2] and references therein) due to the efficiency of the microfabrication process for generating embedded channel waveguides in materials which are known to be difficult to process at the micron and sub-micron scale, especially below surface within embedded volumes. There are at least four characteristics which make ultrashort pulse laser 3DLW CWs unique in comparison with other microfabrication techniques: (i) the CWs are easily engineered so as to guide at any given wavelength within the whole transparency window of these materials (typically from the UV up to the mid-infrared in crystals such as lithium niobate) [3], (ii) the easiness for achieving circular modes as well as single mode behaviour [1, 3, 4], (iii) the particularity that the guiding region is constituted by unmodified pristine material which maintains all the properties of the original optical crystal [3, 5], and (iv) the possibility for writing 3D waveguide architectures inside crystals. These four features undoubtedly enable a wide applications window, for example in the development of linear optical devices for light management, such as beam couplers or interferometers [6], to novel waveguide lasers with gain materials such as rare-earth doped laser crystals [1, 3–5, 7], and nonlinear applications such as parametric frequency conversion processes [8].

There is however an important bottleneck which impedes this development, which is the complete absence of a reliable method to design and fabricate this type of waveguides due to the fact that unknown index change processes take place depending on a wide range of parameters such as the crystals photo-modification sensitivity, the pulse characteristics, and the writing speeds and densities of fabricated volume structures. These characteristics involve complex nonlinear light-matter interaction processes such as nonlinear ionization processes, defect generation, micro-stress induced stress-optic index changes, and others [9]. Presently, a prediction of final material changes subsequent to all these processes is impossible, and therefore fabrication processes typically rely on trial and error multistep fabrication processes.

Furthermore, the refractive index cross-section of these microstructured waveguides is remarkably complex, and it is in fact typically completely un-known due to the lack of index profiling techniques with both the required nanometric resolution and the range of wavelengths of interest (UV to mid-IR). Our goal is to obtain a method to retrieve local refractive index change values across the fabricated structures so as to reliably simulate the behaviour of CWs at different wavelength ranges of operation.

We fabricate 3D CWs elements, such as splitters and combiners with different 3D architectures, and then having converged on a design which gives the best results, we process

Optical Materials EXPRESS

the experimental data such as near-field mode profiles and waveguide propagation losses to infer the local cladding microstructures at the wavelength of testing. We thus report on the development of a method for obtaining the complex index of refraction profiles of $LiNbO_3$ crystalline micro-structured cladding waveguides for the near-IR range. This method allows us to know the waveguide microstructure with a spatial resolution and at a wavelength which is currently impossible to be obtained by any other means. The simulated waveguide modes match well the experimental fundamental mode profiles and their propagation losses, and predict with good agreement other possible higher order modes.

2. Experimental setup

2.1 Waveguide fabrication

A Ti:Sapphire femtosecond laser system with a regenerative amplifier (Spitfire, Spectra-Physics) was used for the 3D Direct Laser Writing (3DLW) of the cladding waveguides. The system produces linearly polarized pulses of ~120 fs duration (Fourier-transform limited), with a repetition rate of 1 kHz at a central wavelength of 795 nm. A calibrated neutral density filter, a motorized half-wave plate and a linear polarizer were used to precisely control the value of the incident-pulse energy. The sample, an optically polished z-cut $LiNbO_3$ sample with dimension of 11(x) × 12(y) × 2(z) mm^3, was mounted on a high-resolution three-axis motorized stage. The laser beam was focused through the xy-plane of the sample (propagation along z-axis) using a microscope objective (50x, N.A. = 0.5). Waveguides were written along the 11-mm long x-axis of the crystal at a constant scanning velocity of 0.35 mm/s and with a pulse energy of 1.9 μJ. Laser polarization was kept perpendicular to the scanning direction (y-axis). For the selected parameters and, under our experimental conditions, damage tracks of around 5 μm in-depth length could be produced in the sample between 100 and 170 μm below sample surface. In this way, a wide range of depths for the fabrication of the waveguides can be exploited keeping constant laser irradiation conditions.

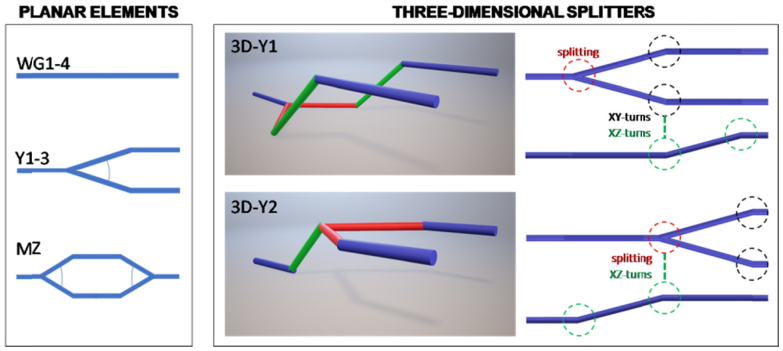

Fig. 1. Schematic diagram of the studied planar and 3D structures.

The design of the circular claddings was done following the approach described in [6] for NdYAG cystal. The procedure consists of fitting the waveguide circumference to a N-side polygon, with a side length of 2 μm. The vertices of the polygon are the coordinates at which the damage tracks will be inscribed along the sample. Firstly, we fabricated straight cladding waveguides with different core radii in order to select the most appropriate, once analyzed the modal behavior and propagation losses. Three radii were considered and analyzed: R = 9 μm (WG1), R = 15 μm (WG2) and R = 20 μm (WG3). Then, based on the R = 9 μm waveguides, some planar waveguide splitting and combining elements were inscribed: straight y-junctions with different splitting angles between arms (0.5° (Y1), 1° (Y2) and 2° (Y3)) and a Mach-Zehnder interferometer architecture with 1° between splitting arms (MZ). The technical strategies for implementing these circuit designs with depressed-index cladding waveguides by means of 3DLW, can be found in [6].

Optical Materials EXPRESS

Following the study of planar elements, 3D versions in which the input and output arms lay at different depths within the sample, were studied. Performing 3D waveguide architectures inside optical crystals is a unique capability of the 3DLW microfabrication technique [10], which allows bringing $LiNbO_3$ waveguides close to surface electrodes for electrooptic modulation [11], and also allows to perform waveguide crossing at different depths with zero cross-talk [12]. In contrast to planar circuit designs, performing 3D circuit architectures opens up a wide range of possible design implementations where different waveguide 3D-path variations can be chosen depending on the specific device purpose and technical constraints. Here, we studied two different 3D-splitter designs to evaluate the impact of each on the splitting losses as well as on the modal output distribution (see Fig. 1). To perform a basic 3D-junction three types of waveguide transitions are required, propagation direction changes in the horizontal plane (XY), in the vertical plane (XZ), and waveguide splitting. We have studied the two possible approaches which maintain the splitting section within the horizontal plane: The first approach (3D-Y1) performs first the beam splitting in the horizontal plane (see red section in Fig. 1), then performs 3D angle changes on each y-branch across both vertical and horizontal planes (red to green section in Fig. 1), and then performs vertical direction changes to redirect the output sections to the horizontal plane. The second approach (3D-Y2) performs first the depth change at the input channel branch (green section in Fig. 1), then performs a simultaneous direction change in the vertical plane and beam splitting within the horizontal plane (a 3D-splitting), and finally corrects the vertical slope of each branch with respective direction changes within the vertical plane. In both cases, a difference of 40 μm in the depth between the input and output arms was chosen, with a splitting angle of 0.5° in the XY plane, and direction changes with angles of ~1° in the vertical XZ plane. However, both designs feature fundamentally different waveguide transitions: the 3D-Y1 design decouples the splitting from vertical turns, in the sense that the y-junction is purely planar and the waveguide division phase doesn't introduce vertical direction. On the contrary, the 3D-Y2 device performs both the beam splitting and the vertical direction changes at the same point (see Fig. 1, right), so that the transition architecture is 3D. Besides the y-junction transitions, each split branch also undergoes different types of bends on each design: in the case of 3D-Y1 each branch performs a direction change in both vertical and horizontal planes, while in the 3D-Y2 design each branch undergo only in-plane direction changes. Since single-mode 3DLW depressed cladding waveguides have been reported to be highly anisotropic [4] as it is also confirmed here, it can be anticipated that each different type of 3D-splitter could have different output properties due to the different designs of the waveguide transitions. We will evaluate the output spatial mode distributions, the splitting ratios, losses, and the field noise in the background space surrounding each output branch.

2.2 Optical waveguide characterization

Output near-field modal profiles and waveguide losses were measured with an end-fire coupling setup with injected light at 633 nm (He-Ne laser) and 850 nm (laser diode). The input beam was focused at the input face of the crystal with a 10X (0.25 NA) microscope objective and the output near-field modal profiles were recorded by imaging the waveguides with a 20X (0.40 NA) microscope objective onto a CMOS camera (IDS uEye SE), measuring the horizontal and vertical mode field diameters (MFDs). The input light polarization was controlled with a linear polarizer and a half-wave plate. To analyze propagation losses (PLs) for either linear horizontal (TE) or vertical (TM) polarizations, an analyzer (polarizer) was placed also after the second microscope objective. PLs of straight waveguides were measured by the scattered-light method [13]. The light (633/850 nm) was injected on each waveguide and the scattered light was imaged by a f = 2 cm lens onto another CMOS camera (IDS uEye SE). From the images, the decay of the transmitted power along the waveguide could be extracted.

Optical Materials EXPRESS

2.3 Design and numerical modelling

The modelling of the fabricated cladding waveguides was performed by means of finite element computational method (FEM hereafter) using the commercial COMSOL software. Our $LiNbO_3$ cladding waveguide model [4] takes into account the anisotropic micro-stress distribution induced by the laser-written tracks [14] using available data for the piezo-optical coefficients of $LiNbO_3$, and also considers the complex index of refraction inside tracks, which is fine adjusted in the model using experimental data values of the propagation losses. To obtain the stress distribution surrounding the cross-section of the waveguides, the local volume changes surrounding a longitudinal and straight laser-written track are numerically calculated with a 2D thermal expansion model, supposing that the amorphized volume inside the tracks expands and elastically distorts the surrounding unmodified crystal. As reported in [4], the model performs a thermal expansion of the tracks to induce an elastic distortion of the longitudinal track surrounding crystalline volume as shown in the equation below, which relates the strain (ε) and stress (σ) tensors and the temperature difference for the linear thermal expansion process:

$$\sigma_{ij} = \sigma_0 + C_{ijkl} : (\varepsilon_{kl} - \varepsilon_0 - \alpha_{kl}\theta). \quad (1)$$

where C_{ijkl} is the 4th order elasticity tensor, ":" stands for the double-dot tensor product, σ_0 and ε_0 are the initial stress and strain, θ is the temperature change parameter controlling the expansion, and α_{kl} is the 2nd order linear thermal expansion tensor (see [4] for further details).

Therefore, in our model we need to input the following numerical parameters to vary the waveguide mode properties: the complex index of refraction inside the tracks $\Delta n^* = \Delta n + i\Delta\kappa$, where Δn is the change in the real part of the index of refraction and $\Delta\kappa$ is the change in the extinction coefficient, and the thermal expansion θ temperature change parameter. While Δn is a value that can be intuitively understood as the change in index of refraction due to defect creation and lattice amorphization, $\Delta\kappa$ can be understood as an increase in absorption of the modified material due to the presence of defects, either absorbing color centers or scattering point defects or both simultaneously. These values are used only inside the laser-written tracks where the femtosecond laser pulses have been tightly focused. Surrounding the tracks, the lattice is assumed to be completely transparent in the un-modified high-quality crystals, and only stress-optic index changes are computed. This approach yields anisotropic index change profiles which agree well with reported experimental characterizations of the anisotropic lattice changes around laser-written tracks [15]. Once a full cladding waveguide refractive index profile is obtained, a detailed mode analysis is performed with an electromagnetic-wave frequency-domain model. All simulations here were calculated for a free space wavelength of 850 nm. The numerical mode calculation gives the near-field distributions of the guided leaky modes, and their corresponding effective indices, which are used to obtain the theoretical mode field diameters (MFDs) and propagation losses (PLs), respectively. Iterative calculations of mode profiles while varying the model input parameters (complex index of refraction inside the tracks and magnitude of the thermal expansion of tracks) are performed until the MFDs and PLs match the experimental values.

3. Results and discussion

In Fig. 2 we show optical microscope images of the fabricated circular cladding waveguides with different radii (upper row).

As it can be seen, laser damage tracks are well defined under white light, and show similar features at the different depths of the structure. Although these tracks appear to have widths of around 1 μm in the optical image, from previous studies under our fabrication conditions [16], we can approximate the real size of the tracks to be of 340 nm in the horizontal cross-section, and 3.4 μm along the vertical direction. This track cross-section is the same one used for numerical modelling of the waveguides.

Optical Materials EXPRESS

The modal behavior was investigated with the end-fire coupling setup. The first observation was that there was a strong dependence in the transmitted power with the polarization of the input laser, with the better transmittance for polarization perpendicular to the laser damage tracks (i.e. TE polarization). In WG1-R9 the fundamental mode (FM) could be easily excited for both 633 nm and 850 nm wavelengths (see Fig. 2(b) and (c)), and a few higher-order modes could be observed after misalignment of the input coupling, this clearly indicating that the waveguide is not strictly single mode. The theoretical laser-written tracks cladding structure of WG1-R9 has also been superimposed over the output modes images for visualization of the relative spatial distribution of cladding and modes.

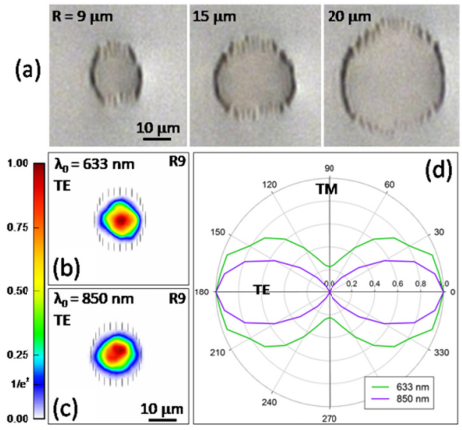

Fig. 2. (a) Optical microscope images of the fabricated waveguides WG1-WG3 (upper row) and (b, c) modal profiles of the WG1-R9 at 633 nm/850 nm. The polarization of the input light was perpendicular to the laser damage tracks (TE polarization). The polar plot (d) represents the normalized transmittance of WG1-R9 for all the polarization directions of the incident light.

The dependence of the waveguide transmittance with the input polarization is depicted in the polar plot of Fig. 2. In the visible the guidance for TM polarization strongly decreases, and in the near IR it almost vanishes to zero. This effect has been previously analysed in detail by Nguyen et al. [4] and it is understood to be a result of the combination of different types of index changes within the cladding structure which play up detrimentally for light polarized along the vertical direction (see further analysis in § IV Numerical Modelling). For larger cladding radii waveguides WG2 and WG3, it was not possible to excite only the FM, and the modal profiles were in all the cases composed by combination of several modes. This effect is probably due to the presence of defects produced during the fabrication that mix the modes in the light propagation though the waveguide.

Table 1. Propagation losses for straight waveguides (dB/cm ± 0.3 dB/cm)

	633 nm		850 nm	
WAVEGUIDE	TE	TM	TE	TM
WG1	2.3	3.8	2.0	-
WG2	2.2	4.1	4.2	-
WG3	3.6	4.8	5.7	-

The measured PLs are summarized in Table 1. At 633 nm both TE and TM polarizations are supported, even though TM polarization show larger losses values for all the waveguides. At 850 nm, only TE polarization is supported and the PLs are found to increase with the

Optical Materials EXPRESS

waveguide radius from 2.0 to 5.7 dB/cm ± 0.3 dB/cm. Since WG1-R9 has the lowest PLs and closest behaviour to a single-mode waveguide, we have selected this for the fabrication of more complex 3D photonic elements, as well as for the in-depth numerical simulation for light at 850 nm, which will give numerical values for the effective index of the FM, as well as an estimation of the complex index of refraction at femtosecond-pulse laser written tracks under our experimental 3DLW microfabrication conditions, which would serve for further optimization of the cladding design from computer simulations without the need to perform extensive trial and error fabrications.

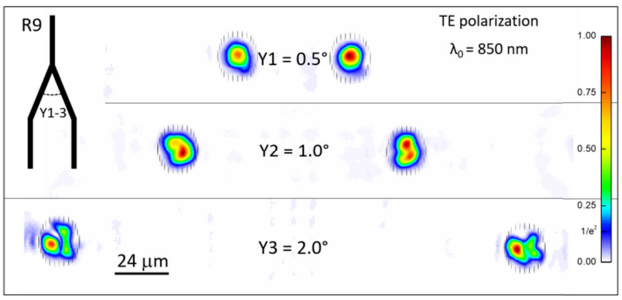

Fig. 3. Modal profiles of the output arms of Y-junctions (Y1-Y3) at 850 nm. The polarization of the input light was perpendicular to the laser damage tracks (TE polarization). The theoretical laser-written tracks cladding structure of WG1-R9 has also been superimposed over the output modes images for visualization of the relative spatial distribution of cladding and modes.

Planar y-junction waveguide splitters were fabricated for divergence angle of the branches of 0.5°, 1.0° and 2.0°. The output near field images of the three different outputs for TM 850 nm wavelength input light are shown in Fig. 3. First it can be seen that between the output modes the cladding light is almost zero, which means that the y-junction design is very effective and a negligible amount of light escapes in the input forward direction. This feature is important in order to have high performance devices. For the case of splitting angle of 0.5° the output modes are seen to maintain the spatial profile of the FM, this meaning that the disturbance of the mode at the junction was minimal and the angle of splitting is well within the numerical aperture of the waveguide. For higher angles of 1.0° however the output fields start to appear mixed with higher order modes, this meaning that the mode transition at the y-junction is not adiabatic and the FM couples to other modes and possibly also radiates light out of the cladding. The higher order modes which are excited appear also to have two intensity maxima along the vertical cross-section.

Finally, for larger divergence angles of 2.0° the output mode distribution is further complicated and higher order modes are excited. Due to the fact that the junction appears to maintain light very well confined within the cladded branches with the field intensity between outputs being almost zero, it could be preliminary concluded that a slight decrease in cladding radius so as to forbid the appearance of higher order modes while maintaining low PLs would correct this detrimental modal noise behavior.

The measured splitting ratios in all the cases were almost equalized but they were very sensitive to the alignment of the input beam [17], which therefore may point to a non-single-mode cladding structure. A similar behavior is found for 633 nm. The transition losses of the y-junctions were evaluated by comparing the total output powers of the two arms ($PY_a + PY_b$) with the output power of WG1 (P0). Then, the additional transition losses of each structure in comparison to those of WG1 are:

$$\eta = -10 \cdot \log_{10}\left(\frac{PY_a + PY_b}{P_0}\right) \tag{2}$$

Optical Materials EXPRESS

The obtained values are summarized in Table 2 for both 633 and 850 nm and TE polarization.

Table 2. Additional losses for y-junctions and MZ (dB)

WAVEGUIDE	TE 633 nm	TE 850 nm
Y1 (0.5°)	4.0	0.3
Y2 (1.0°)	4.7	0.9
Y3 (2.0°)	6.3	3.5
MZ (1.0° x2)	6.6	2.3

Results are reasonably good for the near-IR and for splitting angles of up to 1°. In a first order approximation, supposing light cone angles of 1.0° as the maximal within the NA of the waveguide we can obtain a NA of ~0.0196 for these waveguides at 850 nm. In the visible, the junction additional losses are higher, with 4.0 dB even for the y-junction with smaller separation. The losses of the Mach-Zehnder interferometer (MZ) were evaluated in a similar way, and results are also shown in Table 2. As it can be seen, additional losses do not dramatically increase with respect to the corresponding y-junction with the same divergence angle (Y2).

So far, all the analysis has been performed for planar circuit elements, where the 3DLW competes with other waveguide fabrication techniques such as ion diffusions or implantation. To obtain a real competitive advantage of 3DLW, the technique has to be applied to 3D waveguide circuits designs. As previously described, y-splitters with 3D architectures were also designed and fabricated, featuring two distinct designs where waveguide joints can be either 2D or 3D, and the input and output are always offset by 40 μm along the vertical z-axis. The modal profiles at 850 nm wavelength for the two designs (3D-Y1 and 3D-Y2) are shown in Fig. 4.

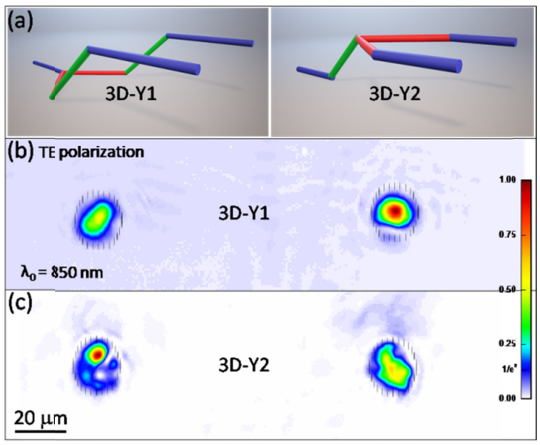

Fig. 4. Modal profiles of the output arms of 3D Y-junctions (3D-Y1, 3D-Y2) at 850 nm. The polarization of the input light was perpendicular to the laser damage tracks (TE polarization). The theoretical laser-written tracks cladding structure of WG1-R9 has also been superimposed over the output modes images for visualization of the relative spatial distribution of cladding and modes.

As previously explained, in principle the most convenient design for a good preservation of the energy within the FM could be the 3D-Y1 (Fig. 4(a)) in which the mode splitting, and

Optical Materials EXPRESS

the depth changes, are done separately. As it is shown in Fig. 4(b), a slight unbalance of the split outputs is observed, but the modal profiles still appear to be within the spatial distribution of the FM.

Moreover, the losses of the splitter (evaluated with the same procedure as in previous structures) do not appreciably increase in comparison with the equivalent planar Y-junction. Featuring an increase of + 0.1 dB at 850nm due to the insertion of the vertical offset transitions (green sections in Fig. 4(a)). The other design where the splitting junction perform both splitting and z-direction changes (3D-Y2), could therefore be expected to feature increased transition losses. Indeed, as it shown in Fig. 4(c) this design exhibits an important energy loss to higher order modes, and a consequent substantial increase in the overall losses (+ 4.2 dB at 850 nm), as shown in Table 3.

Table 3. Additional losses for 3D and y-junctions (dB)

WAVEGUIDE	TE 633 nm	TE 850 nm
3D-Y1	4.5	0.4
3D-Y2	4.4	4.5

4. Numerical modelling

To understand the origin of the highly anisotropic behavior of the fabricated waveguides, and gain a deeper knowledge on the detailed index cross-section of these waveguides for future implementation of design improvements, a detailed numerical simulation of the FM at 850 nm wavelength of WG1-R9 was performed.

Initial parameters for calculating waveguide modes were set as $\Delta n^* = -2\text{x}10^{-3} + \text{i}\cdot 7\text{x}10^{-4}$, which are realistic starting values for 3DLW tracks in crystals following our previous studies [4], and a medium temperature change value θ = 100 K so as to induce stress fields and associated stress-optic change distributions across the cladding. Once an index profile is obtained the fundamental mode is calculated, its theoretical PL is evaluated against the experimental value, the $\Delta\kappa$ at tracks is modified so as to better match it, and finally when calculated and measured PLs do match, the vertical and horizontal MFDs are measured at both intensity full width half maximum (FWHM) and at $1/e^2$ values, and are then compared with the experimental ones.

For this work we first measured the simulated horizontal FWHM and $1/e^2$ MFDs for different values of the index change Δn_o at tracks, spanning low values from $-2\text{x}10^{-3}$ to extreme values of −0.5. The horizontal cross-section is chosen as a fast output parameter which has a direct relationship with the index contrast at tracks, which for the case of the horizontal cross-section of the waveguide is particularly critical due to the fact that for this direction the cladding thickness is as thin as the tracks themselves, and therefore index contrast has a high influence on mode diameter. The resulting horizontal MFDs were then confronted with the experimentally measured ones, and Fig. 5 shows the resulting values. As it can be seen, a gradual mode compression is exerted as the negative index change is increased inside the tracks, increasing the light confinement capability of the depressed index microstructured cladding. The Δn_o at tracks which match the real measured MFDs are however dissimilar for diameters measured at FWHM and $1/e^2$ intensity values of the mode. This can be expected since matching the full profile of the leaky mode is certainly not feasible in a simple approach.

To refine the simulation, an intermediate value for the index change $\Delta n = -0.0075$ at tracks was adopted which best matches both FWHM and $1/e^2$ horizontal MFDs, and then the role of the stress-fields was studied as a second effect to control the FM spatial distribution and cross-section. To obtain realistic values for the level of stress within the cladding, the

Optical Materials EXPRESS

vertical MFD was chosen, which is extremely sensitive to the accumulated stress in the top and bottom parts of the cladding were most tracks are close packed together, producing a characteristic stress compression in the apexes and dilation between tracks, for light polarized perpendicular to the tracks (TE). The lattice dilation between tracks reinforces the depressed cladding effect at the top and bottom of the cladding, although at the track apexes opposite index changes occur, which further complicate the cladding index profile. A set of different levels of cladding microstress was simulated, for which θ was varied from 20 to 400 K values, giving rise to very distinct FM profiles. For each value of θ the $\Delta n = -0.0075$ was maintained, but $\Delta\kappa$ had also to be varied in turn, due to the fact that different modes have different extensions into the cladding structures and therefore propagation losses vary consequently.

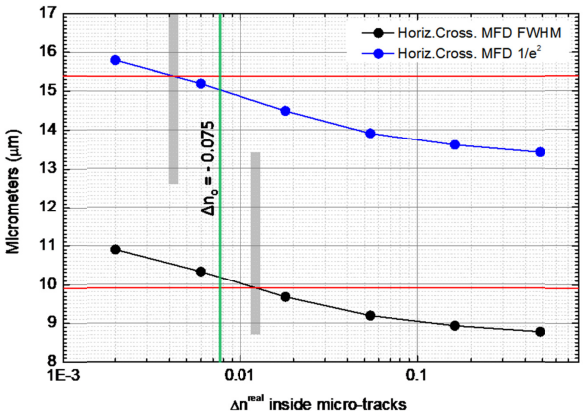

Fig. 5. Calculated horizontal MFDs at different intensity levels for different corresponding Δno values inside the cladding tracks. Horizontal red lines mark the experimentally measured values of the horizontal MFD of WG1-R9 at 850 nm and TE polarization.

Figure 6 summarizes the vertical MFDs against microstress levels for constant PLs = 2 dB/cm as measured (see results before). As it is seen, a very good agreement is found for both values of the vertical MFD is found for θ = 150 K.

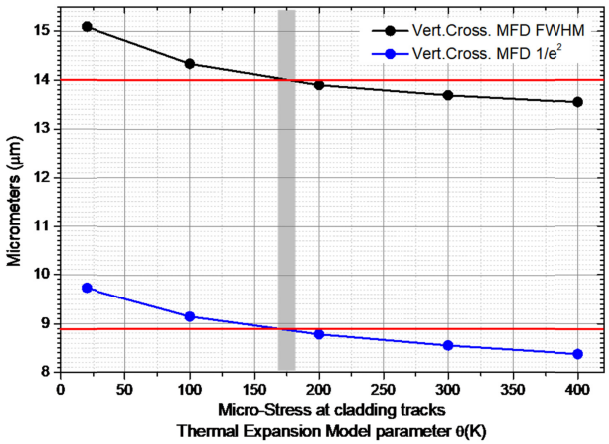

Fig. 6. Calculated vertical MFDs for different corresponding micro-stress values in the cladding waveguide WG1-R9.

Having matched both horizontal and vertical measured MFDs and measured PLs, we have obtained a final FM effective index of $n_{eff} = 2.249187 + i\cdot 3.103\text{x}10^{-6}$, and a change in the complex index of refraction at tracks of $\Delta n^* = -7.5\text{x}10^{-3} + i\cdot 1.17\text{x}10^{-3}$. Figure 7 summarizes

Optical Materials EXPRESS

the numerical simulation of the waveguide. The Δn^* at laser-written tracks corresponds to TE (n_o) light polarization at 850 nm wavelength. Since no output modes could be measured for TM polarization no information could be obtained for the index profile for that polarization. However, it has been previously reported by Burghoff et al. [18] that single laser-written tracks have a relationship between both index of refractions following $\Delta n_e \sim 0.25 \times \Delta n_e$, which was measured for visible light. From this we can therefore infer that for TM polarization the fabricated WG1-R9 has a much reduced index contrast, as well as a positive change in the index of refraction between tracks (qualitatively equal but opposite in sign to the stress-optic changes shown between tracks in Fig. 7(b)), which therefore further weakens the depressed cladding confinement. We therefore conclude that the reason for which extremely high losses were observed for TM light polarization could be these two combined effects.

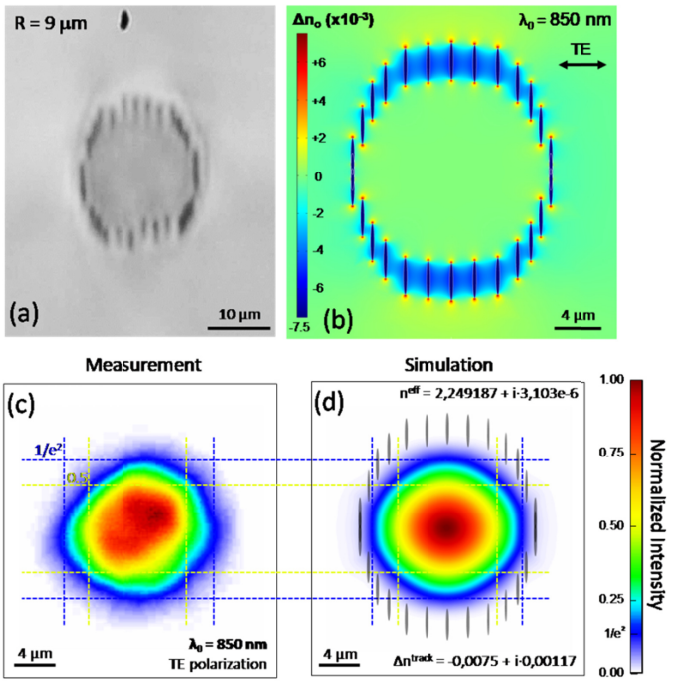

Fig. 7. (a) Optical microscope transmission picture of WG1-R9 cladding waveguide, (b) 2D-index profile obtained after modelling the waveguide properties for the FM, TE polarization at 850 nm wavelength, (c) and (d) experimental and simulated FM near-field intensity distributions, where the 1/e2 and FWHM intensity levels are shown to match. Differences between the circular shape between the two modes are expected to be due to micro-tracks position fluctuations which are not present in the ideal simulated case. The theoretical laser-written tracks cladding structure of WG1-R9 has also been superimposed over the output modes images for visualization of the relative spatial distribution of cladding and modes.

As shown by Nguyen et al. [4] for mid-infrared wavelengths, a way to reach low-losses for both TE and TM polarizations could be by designing a thick cladding along all directions and augmenting the number of tracks so that a highly dense depressed cladding is obtained. Further work in this line is being performed by the authors to further prove this line of research towards low loss cladding waveguides for the near-IR range.

5. Conclusion

In summary, we have been able to successfully fabricate and optimize integrated 3D photonic elements in $LiNbO_3$ based on circular cladding waveguides. Our results indicate the suitability and potential of cladding waveguides fabricated by femtosecond laser irradiation for the implementation of complex 3D photonic circuits for both the visible and near-infrared

Optical Materials EXPRESS

with very good performance. The numerical model developed in this work allows the precise reconstruction of the refractive index profile produced with the femtosecond laser in the crystal, that is essential for the optimization of the structures and for the accurate simulation of other complex photonic elements.

Funding

Junta de Castilla y León (SA046U16); MINECO (FIS2013-44174-P, FIS2015-71933-REDT, FIS2017-87970-R); National Natural Science Foundation (grant No. 61775120); European Union's Horizon 2020 research and innovation program under the Marie Skłodowska-Curie Individual Fellowship (grant No. 747055).